NANO LETTERS

pubs.acs.org/NanoLett Letter

Light-Driven Magnetic Encoding for Hybrid Magnetic Micromachines

Huan Wang,[○] Bin-Bin Xu,[○] Yong-Lai Zhang,* Pavana Siddhartha Kollipara, Shaofeng Liu, Linhan Lin,* Qi-Dai Chen, Yuebing Zheng, and Hong-Bo Sun*

Cite This: *Nano Lett.* 2021, 21, 1628−1635 Read Online

ACCESS | Metrics & More | Article Recommendations | Supporting Information

ABSTRACT: Remote manipulation of a micromachine under an external magnetic field is significant in a variety of applications. However, magnetic manipulation requires that either the target objects or the fluids should be ferromagnetic or superparamagnetic. To extend the applicability, we propose a versatile optical printing technique termed femtosecond laser-directed bubble microprinting (FsLDBM) for on-demand magnetic encoding. Harnessing Marangoni convection, evaporation flow, and capillary force for long-distance delivery, near-field attraction, and printing, respectively, FsLDBM is capable of printing nanomaterials on the solid-state substrate made of arbitrary materials. As a proof-of-concept, we actuate a 3D polymer microturbine under a rotating magnetic field by implementing γ-Fe_2O_3 nanomagnets on its blade. Moreover, we demonstrate the magnetic encoding on a living *daphnia* and versatile manipulation of the hybrid *daphnia*. With its general applicability, the FsLDBM approach provides opportunities for magnetic control of general microstructures in a variety of applications, such as smart microbots and biological microsurgery.

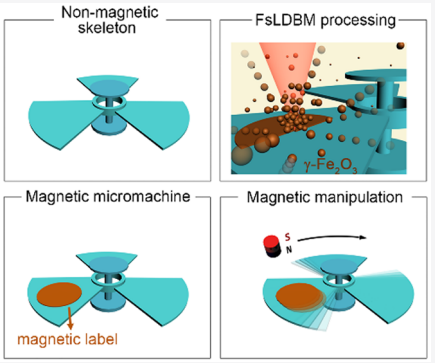

KEYWORDS: *Magnetic manipulation, Optical printing, Microbubbles, Micromachines*

Remote and versatile control of tiny objects has been a long-standing goal in the development of intelligent machines at micro- or nanoscales, which enables a variety of applications in both materials science and life science.[1−6] Micromachines are actuated under external stimuli, where chemical,[7,8] electromagnetic,[9−14] electric,[15−17] acoustic,[18−20] or thermal energies,[13] are converted into kinetic energy of the microengines. Specifically, magnetic micromachines feature excellent biocompatibility as it can freely penetrate biological tissues and has proven noninvasive to the human body. In the past decades, magnetic helical micromotors and tubular micromotors have exhibited intriguing applications in cargo delivery and drug injection.[21−25] It has also been demonstrated that the magnetic micromotors can trap and transport biological cells by controlling the motion modes of the micromotors or incubating the cells to fabricate biohybrid micromotors.[26−29] Moreover, magnetic nanotweezers have been developed to manipulate biomolecules with precise spatiotemporal control, with careful design of the magnetic nanoparticles integrated with biomolecules.[30]

Generally, the actuation of magnetic micromachines stems from positive magnetophoresis, which requires that the target objects be composed of ferromagnetic or superparamagnetic materials. The magnetic manipulation of nonmagnetic objects is still challenging. Several strategies have been proposed so far. For example, nonmagnetic particles were placed in medium with high magnetic susceptibility, where the index-matched nonmagnetic particles are attracted toward the low-field regions by negative magnetophoretic force.[31,32] However, these magnetrofluidic tweezers require either a paramagnetic salt solution or magnetic nanoparticle dispersions to create the magnetrofluidic environment. Another strategy is to attach magnetic materials to nonmagnetic targets. For example, the coating of Ni/Ti bilayers on the three-dimensional (3D) soft architectures provides biocompatible magnetic micromachines for targeted cargo delivery.[21,23,27,29,33] Moreover, the doping of magnetic nanomaterials into photoresist followed by two-photon lithography provides another approach to fabricate hybrid magnetic micromachines.[34,35] Nevertheless, these existing pretreatment techniques lack selectivity and cannot be directly applied to living objects.

Herein, we develop an optical technique, femtosecond laser-directed bubble microprinting (FsLDBM), to achieve on-demand and programmable printing of nanomagnets onto a variety of nonmagnetic structures. Harnessing multiphoton absorption of the femtosecond laser pulse, Marangoni convection-directed massive delivery, and surface tension-

Received: October 19, 2020
Revised: February 3, 2021
Published: February 8, 2021

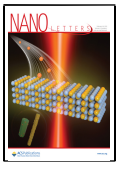

https://dx.doi.org/10.1021/acs.nanolett.0c04165
Nano Lett. 2021, 21, 1628−1635

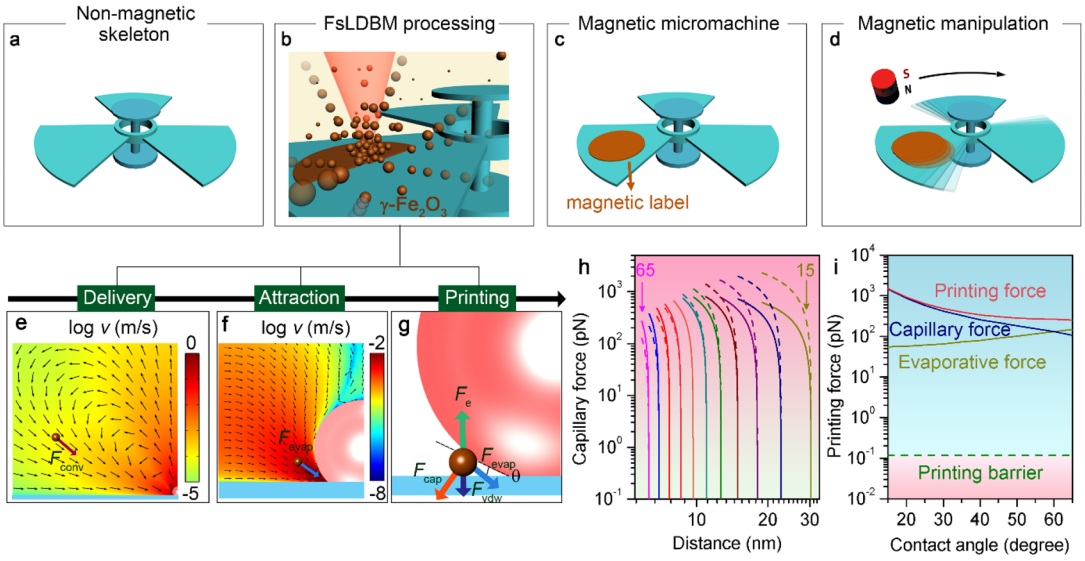

Figure 1. Concept of the on-demand magnetic encoding and working principle of FsLDBM. (a) Schematic of micromachine skeleton made of nonmagnetic materials; (b) printing of γ-Fe_2O_3 nanomagnets on the nonmagnetic skeleton via FsLDBM approach; (c) magnetic functionalization of the micromachines; (d) versatile magnetic manipulation of the micromachine under an external magnetic field. (e) The simulated convective flow from a 2 μm bubble for long-distance delivery of nanoparticles. F_{conc} indicates the convective drag force exerted on the particle. (f) Simulated evaporation flow around the bubble, which attracts the particles toward the three-phase contact line from the vicinity of the bubble. (g) Printing force analysis on the nanoparticle. F_{cap}, F_{vdw}, and F_e represent the capillary force, the van der Waals force, and the electrostatic force, respectively. (h) Calculated capillary force as a function of the particle location, which is described as the distance between the particle center and the bubble-substrate contact point. From left to right, the curves with different colors represent the capillary forces calculated at different contact angles from 65 degrees to 15 degrees, with an interval of 5 degrees. The solid and dashed curves represent the horizontal and perpendicular components of the capillary force (i.e., $F_{cap}^{\parallel}$ and $F_{cap}^{\perp}$), respectively. (i) The printing force as a function of the contact angle and its decomposition of capillary force and evaporative force. The dashed line gives the maximum repulsive force including the electrostatic interaction and van der Waals interaction between the particle and the substrate. A particle size of 8 nm in diameter is taken as an example in the force analysis.

induced printing force, FsLDBM is capable of printing nanoparticles of diverse sizes and materials into free-form micropatterns regardless of the light absorption properties of the substrate. As a proof-of-concept, we demonstrate the magnetic encoding on a 3D polymer microturbine and its actuation under an external magnetic field. More interesting, the general applicability of FsLDBM allows direct magnetic encoding and versatile manipulation of biological objects.

FsLDBM for On-Demand Magnetic Encoding. Figures 1a–d illustrate the concept of on-demand magnetic encoding using FsLDBM and the manipulation of the hybrid magnetic micromachines. The skeleton of the micromachine is composed of nonmagnetic materials (Figure 1a). To enable its magnetic response, we print magnetic nanoparticles (γ-Fe_2O_3 nanomagnets, see Supplementary Figure 1 and Supplementary Note 1) onto the skeleton using FsLDBM (Figure 1b), which acts as the magnetic module to overcome the intrinsic magnetic inability of the original skeleton (Figure 1c). Under an external magnetic field, the magnetic module experiences positive magnetophoretic forces, and the kinetic energy is transferred to the nonmagnetic part to actuate the whole machine (Figure 1d).

Working Principle of FsLDBM. The key to magnetic manipulation of micromachines is to incorporate magnetic nanoparticles onto the nonmagnetic skeleton. Although it has been demonstrated that optical printing can be achieved by harnessing optical scattering force[36−38] or thermophoresis,[39−41] they are limited to specific particles or low throughput. Inkjet printing is a versatile technique, while its printing resolution is low.[42] Bubble printing is a promising technique that is based on an optically controlled microbubble and its interaction with the particle suspension. Nevertheless, the existing bubble printing technique is still limited by its dependence on light-absorbing materials, i.e., either the substrate[43−46] or the target nanoparticles[47,48] has relatively high light absorption efficiency in converting energy from light to heat. In previous work, it has been pointed out that the capillary flow dominates the particle deposition at the edge, and controlling the relative magnitude of Marangoni flow significantly modifies the thickness distribution of the deposited thin film during the evaporation of a droplet.[49] However, the underlying mechanism of bubble printing remains unclear.

Herein, we propose to use a femtosecond laser for microbubble generation and nanoparticle printing. It has been previously demonstrated that the use of a femtosecond laser beam leads to the optical breakdown of purified water and the generation of cavitation bubbles. Moreover, the generated bubble can be trapped by the self-focused laser beam.[50] In this work, we irradiated a femtosecond laser onto solvent/substrate interface, where the multiphoton absorption of water molecules leads to water evaporation and subsequent nucleation and growth of steam bubbles. The microbubble captures the suspended particles, delivers them to the bubble surface, and prints them onto the solid-state substrate (Figure 1b, also see Supplementary Video 1). It should be noted that the heating of bulk water at the same optical power cannot lead to bubble generation, indicating that the existence of a water-substrate interface enhances the optical intensity or reduces the nucleation threshold. In contrast to continuous-wave laser, the use of femtosecond laser releases the rigorous material requirement of the substrate and the target particles, i.e.,

https://dx.doi.org/10.1021/acs.nanolett.0c04165
Nano Lett. 2021, 21, 1628−1635

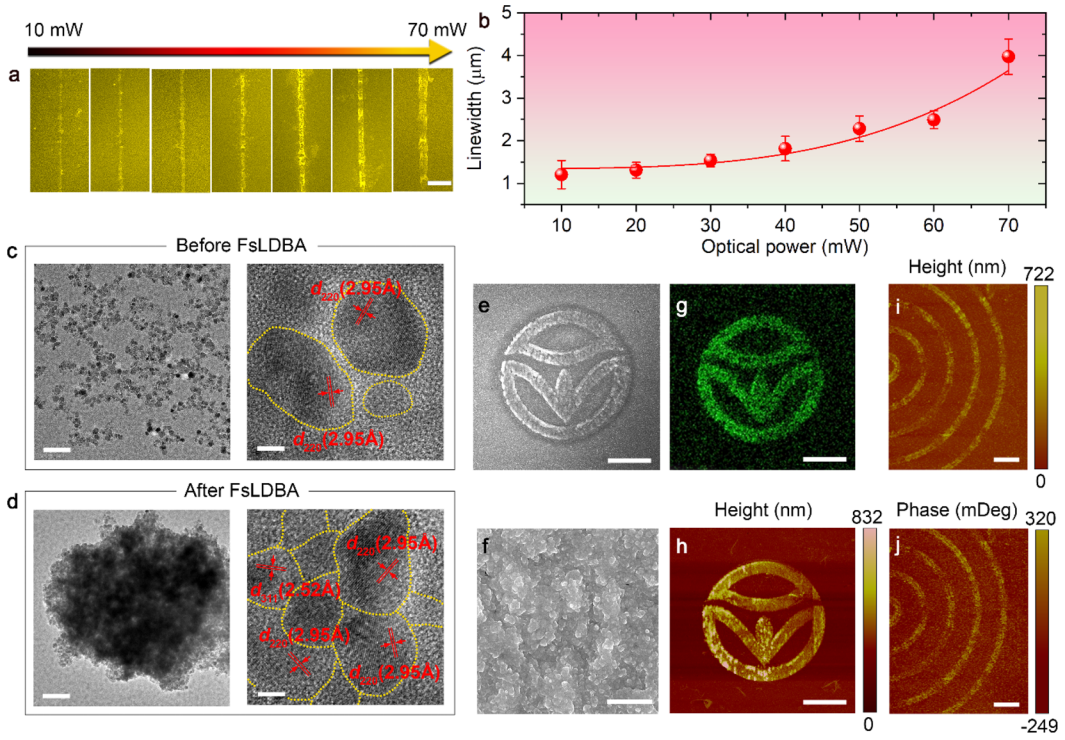

Figure 2. Diverse printing capability of FsLDBM. (a) SEM images of the line patterns of γ-Fe_2O_3 nanomagnets printed at different optical powers. Scale bars: 10 μm. (b) The line widths of the printed line patterns as a function of the optical powers. The data is fitted with a function $y = y_0 + Ax^B$, where y_0 = 1.35, $A = 1.27 \times 10^{-6}$, B = 3.39. (c) TEM images of the magnetic nanoparticles before FsLDBM. (d) TEM images of the magnetic nanoparticles after FsLDBM. (e–h) SEM images, Fe elemental map, and AFM image of a "green food" logo printed with γ-Fe_2O_3 nanomagnets: low magnification SEM image (e); high magnification SEM image (f); EDS mapping of Fe element (g); AFM image of the "green food" logo (h). (i–j) Magnetic force microscopy image of a multiple-ring pattern of γ-Fe_2O_3 nanomagnets showing the thickness (i) and the magnetic intensity (j). Scale bars: 10 μm (panels a, e, g–j); 50 nm (left panel in c); 100 nm (left panel in d); 5 nm (right panels in c and d); 1 μm (f).

both light-absorbing and nonabsorbing materials are workable, which extends the applicability of FsLDBM.

In order to understand the printing mechanism, we analyzed the force exerted on the particles at different locations, as illustrated in Figures 1e–g. Upon laser irradiation, the temperature gradient at the bubble surface induces Marangoni convection to deliver the nanoparticles toward the laser spot (Figure 1e), with the drag force on the suspended particles given by[43,51]

$$F_{\mathrm{conv},r} = m_{\mathrm{p}}\left(u_r\frac{\partial u_r}{\partial r} + u_z\frac{\partial u_r}{\partial z}\right) \quad (1)$$

$$F_{\mathrm{conv},z} = m_{\mathrm{p}}\left(u_r\frac{\partial u_z}{\partial r} + u_z\frac{\partial u_z}{\partial z}\right) \quad (2)$$

where F_{conv} indicates the convection-induced accelerative force, the subscripts r and z indicate the radial direction toward the bubble center and axial direction perpendicular to the substrate, respectively. m_{p} indicates the mass of the particle, and u represents the nanoparticle velocity. Here, the nanoparticle is considered as a point particle as the variation in velocity caused by the nanoparticle is ignorable. The maximum flow velocity of 10^{-1} m/s allows high-speed transport of suspended nanoparticles toward the bubble.

When the particle is in the vicinity of the bubble surface, near-field evaporation of water around the solid–liquid–vapor three-phase contact line will drive the nanoparticle toward the bubble surface (Figure 1f), with a mass flux $\vec{m} = \frac{P}{h_{\mathrm{l}}}$, where P is the absorbed optical power and h_{l} is the latent heat of water evaporation, taken at standard conditions. The simulated evaporative flow around the bubble is given in Figure 1f, with a maximum evaporative flow of 10^{-2} m/s obtained. As the nanoparticle approaches the three-phase contact line, the flow is altered by the nanoparticle, and the bulk velocity around the particle becomes nonuniform. Therefore, full-scale three-dimensional simulations have been carried out to determine the force from the total stress, including both the viscous stress (drag force) and the pressure (lift force) on the particle (see Supplementary Figure 2 and Supplementary Note 2). For ease of simulation, we performed the force analysis at the stationary state when the particle touches the surface to neglect the effect of particle motion on the force it experiences due to evaporation.

Once the particle touches the bubble surface, it deforms the surface due to the radially inward evaporative forces, leading to an opposing reaction force, which is known as capillary force or surface tension force:[52]

$$F_{\mathrm{cap}} = 4\pi\gamma r_{\mathrm{p}}\left(1 - \sin\left(\theta + \sin^{-1}\frac{d - r_{\mathrm{p}}}{r_{\mathrm{p}}}\right)\right) \quad (3)$$

where γ is the surface tension of the bubble surface, d is the particle-to-substrate distance, θ is the contact angle, and r_{p} is the particle radius. As the bubble surface is oblique to the substrate, the capillary force has a horizontal and a perpendicular component ($F^{\parallel}_{\mathrm{cap}}$ and $F^{\perp}_{\mathrm{cap}}$, respectively). While $F^{\parallel}_{\mathrm{cap}}$ balances the horizontal component of evaporative force $F^{\parallel}_{\mathrm{evap}}$ which points inwardly, the perpendicular components of both capillary force $F^{\perp}_{\mathrm{cap}}$ and evaporative force $F^{\perp}_{\mathrm{evap}}$ overcome

https://dx.doi.org/10.1021/acs.nanolett.0c04165
Nano Lett. 2021, 21, 1628–1635

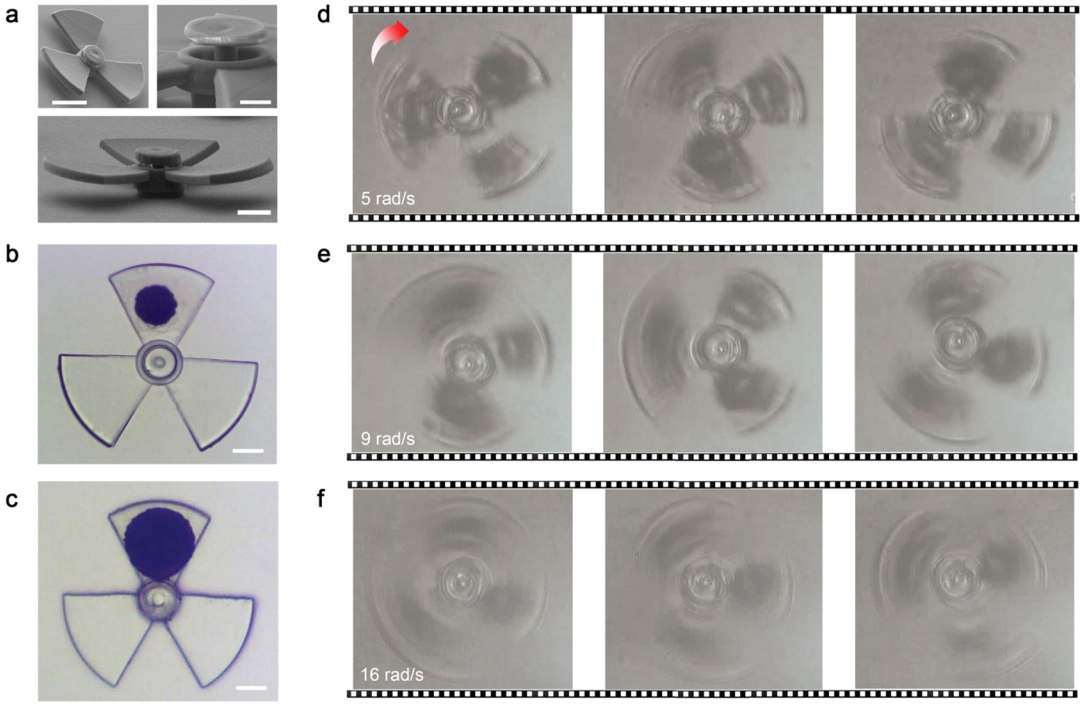

Figure 3. 3D magnetic microturbine. (a) SEM images of the 3D polymer microturbine. (b, c) Optical images of the 3D magnetic microturbine after the printing of γ-Fe_2O_3 nanomagnets with different sizes. (d–f) Rotation of the 3D magnetic microturbine at different velocities: 5 rad/s (d); 9 rad/s (e); 16 rad/s (f). Scale bars: 20 μm (left panel at the top and bottom in panels a–c); 5 μm (right panel at the top in panel a).

the electrostatic repulsive force F_e from the substrate, and helps to print the particle along with van der Waals force F_{vdw} (Figure 1g). We can see that $F_{cap}^{\perp}$ is more significant at a smaller contact angle (Figure 1h). We further calculate the electrostatic interaction and van der Waals interaction (Supplementary Note 2), giving the overall printing force and repulsive force (Figure 1i). The repulsive barrier of an 8 nm γ-Fe_2O_3 nanoparticle is 118 fN. The evaporative force is always directed to the three-phase contact line, while the capillary force is perpendicular to the bubble surface. Thus, at smaller angles, the printing force is dominated by the capillary force. As both forces are individually much higher than the repulsive barrier, printing takes place at all contact angles, with the maximum printing force above 1 nN. Although the capillary force is the major printing force, it is not the particle–substrate bonding force. When the laser is turned off, all these light-generated forces disappear, while the van der Waals interaction takes charge and the nanoparticles are assembled on the interface permanently. Moreover, the printed particles become parts of the substrate and the interparticle connection, which leads to nanoparticle assembly, and can be explained in the same model by replacing the particle–substrate interaction with interparticle interaction.

Diversity of FsLDBM. On the basis of the understanding of the working principle, we further examine the diversity of FsLDBM. As shown in Figure 2a, we printed the γ-Fe_2O_3 nanomagnets into line patterns at different optical powers and examined the scanning electron microscope (SEM) images. The line width of the printed patterns is a function of the bubble size, which is determined by the optical power and the distribution of the thermal hot spots. A line width of ~1.2 μm is observed at an optical power of 10 mW, while it increases with the optical power. The printing resolution as a function of the optical power is summarized in Figure 2b, where the fitting reveals that the line width shares a power relationship with the optical power. Different from a continuous-wave laser, the use of femtosecond laser leads to nonlinear absorption for heat generation, which creates a more localized thermal hot spot and improves the printing resolution. Optimization of the laser spot generates submicron bubbles, with a printing resolution of ~500 nm achieved (Supplementary Figure 3).

To investigate the morphologic and structural change of the γ-Fe_2O_3 nanomagnets during FsLDBM, we analyzed the transmission electron microscope (TEM) images of the γ-Fe_2O_3 nanomagnets before and after FsLDBM (Figure 2c,d). Without FsLDBM, the γ-Fe_2O_3 nanomagnets are well dispersed and separated from each other. The interparticle gap is unobservable in the TEM images after FsLDBM (Figure 2d), indicating that the nanoparticles are bonded tightly by van der Waals force. Moreover, we observed a constant lattice spacing of (220) crystal plane (d_{220} = 2.95 Å) in Figure 2c,d, revealing that the crystalline structure of the nanoparticles was well maintained during the FsLDBM processing.

Taking advantage of the flexibility in light management, we are capable of printing nanoparticles into arbitrary patterns. As an example, we have printed the γ-Fe_2O_3 nanomagnets into a "green food" logo (Figure 2e). The high-magnification SEM image reveals a close-packed feature (see Figure 2f), which is consistent with the energy dispersive spectrometry (EDS) of the Fe element (Figure 2g). The atomic force microscopy (AFM) image gives a maximum thickness of 832 nm (Figure 2h). It is noted that the integrity of the micropatterns relies on the evolution of the microbubbles during printing, while the independence on the light-absorbing substrate in FsLDBM improves the bubble stability and integrity. We have also created a γ-Fe_2O_3 multiple-ring pattern and characterize the morphology and the magnetic intensity using a magnetic force microscope. As shown in Figure 2i,j, the magnetic intensity is

https://dx.doi.org/10.1021/acs.nanolett.0c04165
Nano Lett. 2021, 21, 1628–1635

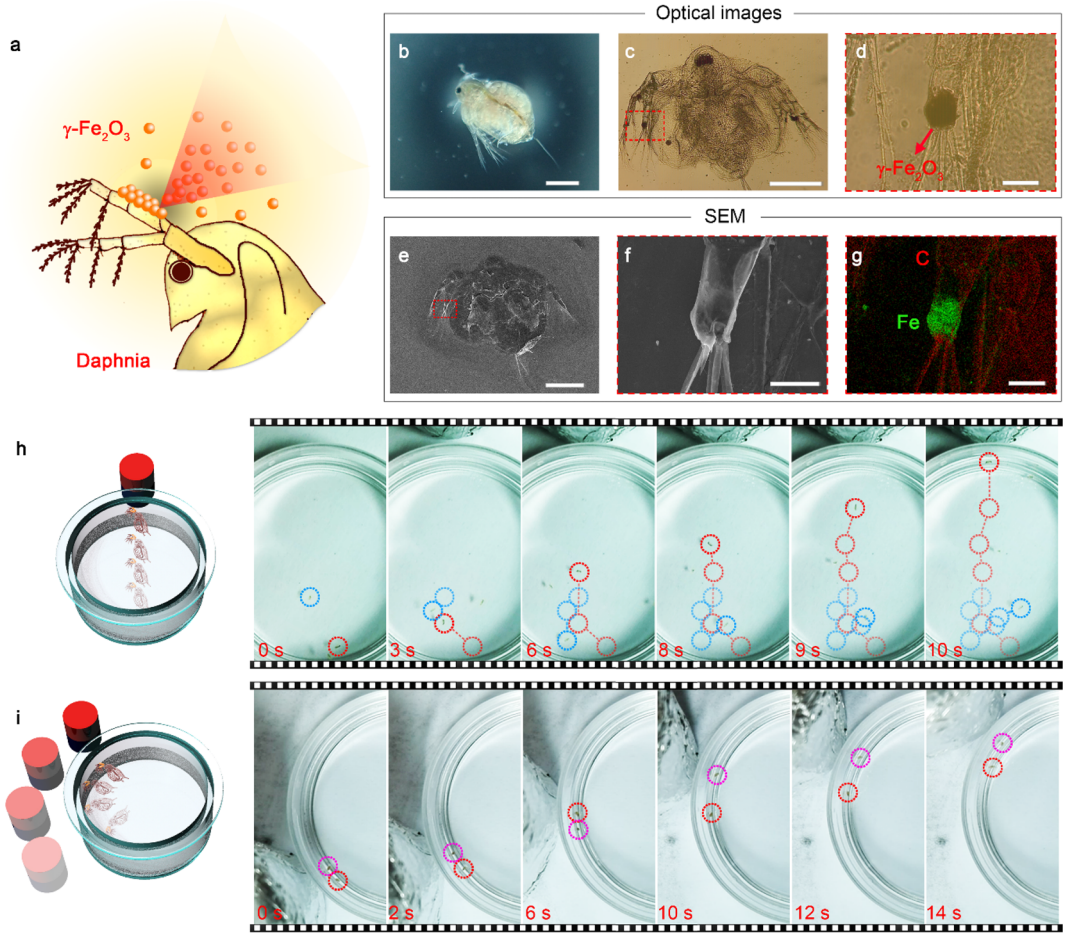

Figure 4. Magnetic manipulation of living *daphnia*. (a) Schematic of a *daphnia* with γ-Fe_2O_3 nanomagnets printed on one of its thoracic appendages. (b) Optical image of a *daphnia* before magnetic functionalization. (c) Optical image of a magnetic *daphnia* after the printing of γ-Fe_2O_3 nanomagnets on one of the thoracic appendages. (d) Optical image of the magnetic thoracic appendage. (e) SEM image of the *daphnia* after the printing of γ-Fe_2O_3 nanomagnets. (f, g) SEM (f) and EDS mapping of Fe and C elements (g) of the magnetic thoracic appendage. (h) Long-distance magnetic trapping of a living *daphnia*. The magnetic *daphnia* manipulated by the external magnetic field is labeled with a red dash circle, while the nonmagnetic *daphnia* is labeled with a blue dash circle. (i) Magnetic rotation of two magnetic *daphnia* by rotating the external magnetic field. The magnetic *daphnia* are labeled with a red dash circle and a pink dash circle, respectively. Scale bars: 400 μm (b, c, e); 40 μm (d, f, g).

proportional to the thickness, revealing that FsLDBM is noninvasive to the magnetic nanomaterials and the magnetic performance is programmable by adjusting the pattern thickness. Moreover, the capillary force is independent of the physical properties of the nanoparticles, which suggests that FsLDBM is applicable to a wide range of materials, such as polymers, metals, and semiconductors. As shown in Supplementary Figure 4, we have digitally printed silver nanoparticles and CdTe quantum dots into a Chinese word of "light" and a "piercing heart" pattern, respectively. The surface coverage, thickness, and homogeneity of the patterns rely on the patterning parameters such as optical power, scanning rate, step size, and particle concentration. A parametric optimization leads to a 2D pattern with a particle density of 1.1×10^{13} cm^{-2} and surface coverage of 96.8% at a thickness of 30 nm (Supplementary Figure 5). Besides the 2D patterning, the use of femtosecond laser provides the possibility for 3D printing, as the microbubble generation at the interface between the printed structure and the nanoparticle suspensions is achievable, where the capillary force helps to fix the suspended particles onto the predeposited particles for 3D connection. As a demonstration, we printed the CdSe/ZnS quantum dots into arc-bridge 3D patterns, with the heights of 10 and 20 μm from the substrate, respectively (see Supplementary Note 1). The laser scanning confocal fluorescence images verify the well-defined 3D configuration of the printed patterns, as shown in Supplementary Figure 6.

Magnetic Manipulation of 3D Polymer Microturbine. The diversity of the FsLDBM allows the on-demand encoding of magnetic nanomaterials onto various nonmagnetic structures. As a demonstration, we fabricated a 3D polymer (poly(butyl methacrylate), PBMA) microturbine using a two-photon polymerization (TPP) technique, as shown in Figure 3a. The microturbine is 100 μm in diameter and 25 μm in height, while the suspended blades are 15 μm above the substrate. The microturbine was then immersed in the γ-Fe_2O_3 solution for magnetic encoding. The size of the functional magnetic module is tunable to modify the magnetic performance. The hybrid microturbine was placed in a magnetic field created by a magnet. The printed magnetic module undergoes positive magnetophoresis along the magnetic field gradient, with the magnetophoretic estimated by $F_M = \chi_p \mu_0 V(\mathbf{H}\cdot\nabla)\mathbf{H}$, where μ_0 is the vacuum permeability, V is the volume of the magnetic module, χ_p is the magnetic susceptibility, $\mathbf{H}$ is the external magnetic field. Through rotating the magnet electrically, the microturbine started to spin. In addition, the rotation

https://dx.doi.org/10.1021/acs.nanolett.0c04165
Nano Lett. 2021, 21, 1628−1635

velocity is tunable by controlling the rotating speed of the magnet, as shown in Figures 3d–f (also see Supplementary Videos 2–4).

Magnetic Manipulation of Living Microorganism. In contrast to the artificial micromachines, where the structure and composition can be precisely tailored, the magnetic control of living objects in nature is still elusive because biomolecules are nonmagnetic, and the incorporation of magnetic materials into living bodies is more challenging. The incubation of biological cells or organisms in a solution containing magnetic micromotors allows the formation of biohybrid micromachines.[27−29,53] For example, it has been demonstrated that the incubation of sperms in magnetic microhelix-suspended solution provides the sperm-carrying micromotors, which allows versatile magnetic manipulation of sperms for assisted fertilization or drug delivery.[28,29] However, the incubation approach normally lacks selectivity and cannot achieve localized magnetic encoding. Herein, taking a living *daphnia* as an example, we demonstrate that FsLDBM can be applied to living microorganisms (Figure 4a). The optical image of a living *daphnia* is shown in Figure 4b. To achieve magnetic functionalization, we selectively printed a γ-Fe_2O_3 micropattern of 40 μm in diameter on one of the thoracic appendages (Figure 4c,d). Different from the glass substrate, the morphology of thoracic appendages is irregular and complex. After FsLDBM, a conformal γ-Fe_2O_3 thin film was deposited on the surface of the thoracic appendage (Figure 4e,f). EDS mapping of the *daphnia* after magnetic encoding is illustrated in Figure 4g. The C element signal arises from the organs of the *daphnia*, while the Fe element represents the functional γ-Fe_2O_3 module. We can see that the Fe signal is uniform crossing the magnetic pattern, although the surface of the thoracic appendage is rough.

We further demonstrate the manipulation of *daphnia* after magnetic encoding. To improve the magnetic force, ten γ-Fe_2O_3 micropatterns were printed on the *daphnia*. The functionalized *daphnia* was then placed in a Petri dish containing DI water. When an external magnetic field is applied, the hybrid *daphnia* was pulled along the magnetic field gradient and trapped at the edge of the Petri dishes. The *daphnia* was released when the magnetic field was off (see Supplementary Video 5 for the real-time manipulation). It should be noted that the volume of the magnetic module is almost 6 orders of magnitude smaller than that of the *daphnia*, while the magnetic force is strong enough to deliver the hybrid *daphnia*. Our calculation estimates a magnetic force from several micronewton to more than 50 micronewton (see Supplementary Note 3 for the calculation detail). As a comparison, a nonmagnetic *daphnia* was also placed in the Petri dish. We can see that the nonmagnetic *daphnia* undergo Brownian swimming under the magnetic field (see the blue dash circles in Figure 4h). Moreover, we also demonstrated the rotation of two magnetic *daphnia* along the edge of the Petri dishes under a rotating magnetic field (see Figure 4i and Supplementary Video 7). It is noted that the microbubble generation may cause thermal damage to the skin of the *daphnia*. To reduce the thermal toxicity, the laser pulse should be modulated to reduce the lifetime of the microbubble and achieve ultrafast bubble evolution dynamics. Different from an optical force, which stems from the refractive index contrast between the target object and the surrounding medium, the light-induced forces in FsLDBM do not rely on the refractive index of the target surface and optical printing of nanoparticles on the membrane of biological cells is possible (Supplementary Figure 7).

In conclusion, we propose a general optical printing technique for long-distance delivery, near-field attraction, and patterning of nanoparticles. Through the coordinated coupling of multiphoton absorption, Marangoni convection, evaporation flow, and capillary effect, FsLDBM breaks the rigorous material requirement in traditional bubble printing techniques and is capable of printing diverse nanomaterials onto the different solid-state substrate. The on-demand encoding of γ-Fe_2O_3 nanomagnets onto diverse nonmagnetic structures such as 3D polymer microturbines and living *daphnia* enables their response to the external magnetic field for remote and noninvasive manipulation. Our work provides an alternative strategy to design magnetic hybrid micromachines for applications such as intelligent robotics and nanomedicine.

■ ASSOCIATED CONTENT

Supporting Information

The Supporting Information is available free of charge at https://pubs.acs.org/doi/10.1021/acs.nanolett.0c04165.

Additional experimental and computational results including X-ray diffraction spectrum and hysteresis loops characterization of the γ-Fe_2O_3 nanoparticles; calculated evaporative force on single γ-Fe_2O_3 nanoparticles; optimized printing line width of FsLDBM; SEM and EDS mapping of micropatterns composed of different materials; SEM images and white light interference microscopy of CdSe/ZnS quantum dot 2D patterns; 3D printing of quantum dots; FsLDBM on the cell membrane, the experimental method, the printing force calculation of FsLDBM, and the calculation of magnetic force on the hybrid *daphnia* (PDF)

The printing of 500 nm polystyrene beads using a single microbubble (MP4)

Real-time magnetic rotation of the functionalized 3D microturbine at a rotation speed of 5 rad/s (MP4)

Real-time magnetic rotation of the functionalized 3D microturbine at a rotation speed of 9 rad/s (MP4)

Real-time magnetic rotation of the functionalized 3D microturbine at a rotation speed of 16 rad/s (MP4)

Real-time magnetic trapping of a living *daphnia* after magnetic functionalization (MP4)

Long-distance magnetic trapping of a living *daphnia* (MP4)

Magnetic rotation of a living *daphnia* along the edge of the Petri dishes (MP4)

■ AUTHOR INFORMATION

Corresponding Authors

Yong-Lai Zhang − *State Key Laboratory of Integrated Optoelectronics, College of Electronic Science and Engineering, Jilin University, Changchun 130012, China;* orcid.org/0000-0002-4282-250X; Email: yonglaizhang@jlu.edu.cn

Linhan Lin − *State Key Laboratory of Precision Measurement Technology and Instruments, Department of Precision Instrument, Tsinghua University, Haidian, Beijing 100084, China;* orcid.org/0000-0003-0556-9143; Email: linlh2019@tsinghua.edu.cn

Hong-Bo Sun − *State Key Laboratory of Precision Measurement Technology and Instruments, Department of*

https://dx.doi.org/10.1021/acs.nanolett.0c04165
Nano Lett. 2021, 21, 1628−1635

Precision Instrument, Tsinghua University, Haidian, Beijing 100084, China; State Key Laboratory of Integrated Optoelectronics, College of Electronic Science and Engineering, Jilin University, Changchun 130012, China; orcid.org/0000-0003-2127-8610; Email: hbsun@tsinghua.edu.cn

Authors

Huan Wang − *State Key Laboratory of Integrated Optoelectronics, College of Electronic Science and Engineering, Jilin University, Changchun 130012, China; Hooke Instruments, Changchun Institute of Optics, Fine Mechanics and Physics, Chinese Academy of Sciences, Changchun 130033, China*

Bin-Bin Xu − *State Key Laboratory of Integrated Optoelectronics, College of Electronic Science and Engineering, Jilin University, Changchun 130012, China*

Pavana Siddhartha Kollipara − *Walker Department of Mechanical Engineering, The University of Texas at Austin, Austin, Texas 78712, United States;* orcid.org/0000-0003-0166-6720

Shaofeng Liu − *State Key Laboratory of Precision Measurement Technology and Instruments, Department of Precision Instrument, Tsinghua University, Haidian, Beijing 100084, China*

Qi-Dai Chen − *State Key Laboratory of Integrated Optoelectronics, College of Electronic Science and Engineering, Jilin University, Changchun 130012, China;* orcid.org/0000-0002-0921-7973

Yuebing Zheng − *Walker Department of Mechanical Engineering and Materials Science & Engineering Program and Texas Materials Institute, The University of Texas at Austin, Austin, Texas 78712, United States;* orcid.org/0000-0002-9168-9477

Complete contact information is available at: https://pubs.acs.org/10.1021/acs.nanolett.0c04165

Author Contributions

○H.W. and B.-B.X. contributed equally to this work.

Notes

The authors declare no competing financial interest.

■ ACKNOWLEDGMENTS

This work was supported by the National Key Research and Development Program of China and National Natural Science Foundation of China (NSFC) under grants nos. 2017YFB1104300, 2020YFA0715000, 61935008, 61590930, 61775078, and 62075111. L.L. acknowledges the financial support from the State Key Laboratory of Precision Measurement Technology and Instruments. Y.Z. and P.S.K. acknowledge the financial support of the National Science Foundation (NSF-CMMI-1761743). We thank Jiatai Huang for the help in the calculation of magnetic force.

■ REFERENCES

(1) Esteban-Fernández de Ávila, B.; Gao, W.; Karshalev, E.; Zhang, L.; Wang, J. Cell-Like Micromotors. *Acc. Chem. Res.* **2018**, *51*, 1901.

(2) Tu, Y.; Peng, F.; Wilson, D. A. Motion Manipulation of Micro- and Nanomotors. *Adv. Mater.* **2017**, *29*, 1701970.

(3) Xu, T.; Gao, W.; Xu, L.-P.; Zhang, X.; Wang, S. Fuel-Free Synthetic Micro-/Nanomachines. *Adv. Mater.* **2017**, *29*, 1603250.

(4) de Ávila, B. E.-F.; Angsantikul, P.; Li, J.; Angel Lopez-Ramirez, M.; Ramírez-Herrera, D. E.; Thamphiwatana, S.; Chen, C.; Delezuk, J.; Samakapiruk, R.; Ramez, V.; Zhang, L.; Wang, J. Micromotor-enabled active drug delivery for in vivo treatment of stomach infection. *Nat. Commun.* **2017**, *8*, 272.

(5) Li, J.; Gao, W.; Dong, R.; Pei, A.; Sattayasamitsathit, S.; Wang, J. Nanomotor lithography. *Nat. Commun.* **2014**, *5*, 5026.

(6) Mano, T.; Delfau, J.-B.; Iwasawa, J.; Sano, M. Optimal run-and-tumble−based transportation of a Janus particle with active steering. *Proc. Natl. Acad. Sci. U. S. A.* **2017**, *114*, E2580.

(7) Dong, R.; Cai, Y.; Yang, Y.; Gao, W.; Ren, B. Photocatalytic Micro/Nanomotors: From Construction to Applications. *Acc. Chem. Res.* **2018**, *51*, 1940.

(8) Ebbens, S. J.; Gregory, D. A. Catalytic Janus Colloids: Controlling Trajectories of Chemical Microswimmers. *Acc. Chem. Res.* **2018**, *51*, 1931.

(9) Wang, J.; Xiong, Z.; Zheng, J.; Zhan, X.; Tang, J. Light-Driven Micro/Nanomotor for Promising Biomedical Tools: Principle, Challenge, and Prospect. *Acc. Chem. Res.* **2018**, *51*, 1957.

(10) Liu, M.; Zentgraf, T.; Liu, Y.; Bartal, G.; Zhang, X. Light-driven nanoscale plasmonic motors. *Nat. Nanotechnol.* **2010**, *5*, 570.

(11) Maggi, C.; Saglimbeni, F.; Dipalo, M.; De Angelis, F.; Di Leonardo, R. Micromotors with asymmetric shape that efficiently convert light into work by thermocapillary effects. *Nat. Commun.* **2015**, *6*, 7855.

(12) Wu, T.; Nieminen, T. A.; Mohanty, S.; Miotke, J.; Meyer, R. L.; Rubinsztein-Dunlop, H.; Berns, M. W. A photon-driven micromotor can direct nerve fibre growth. *Nat. Photonics* **2012**, *6*, 62.

(13) Schmidt, F.; Magazzù, A.; Callegari, A.; Biancofiore, L.; Cichos, F.; Volpe, G. Microscopic Engine Powered by Critical Demixing. *Phys. Rev. Lett.* **2018**, *120*, 068004.

(14) Ahn, J.; Xu, Z.; Bang, J.; Deng, Y.-H.; Hoang, T. M.; Han, Q.; Ma, R.-M.; Li, T. Optically Levitated Nanodumbbell Torsion Balance and GHz Nanomechanical Rotor. *Phys. Rev. Lett.* **2018**, *121*, 033603.

(15) Boymelgreen, A. M.; Balli, T.; Miloh, T.; Yossifon, G. Active colloids as mobile microelectrodes for unified label-free selective cargo transport. *Nat. Commun.* **2018**, *9*, 760.

(16) Liang, Z.; Fan, D. Visible light−gated reconfigurable rotary actuation of electric nanomotors. *Sci. Adv.* **2018**, *4*, No. eaau0981.

(17) Fan, D. L.; Zhu, F. Q.; Cammarata, R. C.; Chien, C. L. Electric tweezers. *Nano Today* **2011**, *6*, 339.

(18) Wang, W.; Li, S.; Mair, L.; Ahmed, S.; Huang, T. J.; Mallouk, T. E. Acoustic Propulsion of Nanorod Motors Inside Living Cells. *Angew. Chem., Int. Ed.* **2014**, *53*, 3201.

(19) Ahmed, D.; Baasch, T.; Jang, B.; Pane, S.; Dual, J.; Nelson, B. J. Artificial Swimmers Propelled by Acoustically Activated Flagella. *Nano Lett.* **2016**, *16*, 4968.

(20) Ren, L.; Nama, N.; McNeill, J. M.; Soto, F.; Yan, Z.; Liu, W.; Wang, W.; Wang, J.; Mallouk, T. E. 3D steerable, acoustically powered microswimmers for single-particle manipulation. *Sci. Adv.* **2019**, *5*, No. eaax3084.

(21) Tottori, S.; Zhang, L.; Qiu, F.; Krawczyk, K. K.; Franco-Obregón, A.; Nelson, B. J. Magnetic Helical Micromachines: Fabrication, Controlled Swimming, and Cargo Transport. *Adv. Mater.* **2012**, *24*, 811.

(22) Huang, T.-Y.; Sakar, M. S.; Mao, A.; Petruska, A. J.; Qiu, F.; Chen, X.-B.; Kennedy, S.; Mooney, D.; Nelson, B. J. 3D Printed Microtransporters: Compound Micromachines for Spatiotemporally Controlled Delivery of Therapeutic Agents. *Adv. Mater.* **2015**, *27*, 6644.

(23) Qiu, F.; Fujita, S.; Mhanna, R.; Zhang, L.; Simona, B. R.; Nelson, B. J. Magnetic Helical Microswimmers Functionalized with Lipoplexes for Targeted Gene Delivery. *Adv. Funct. Mater.* **2015**, *25*, 1666.

(24) Yan, X.; Zhou, Q.; Yu, J.; Xu, T.; Deng, Y.; Tang, T.; Feng, Q.; Bian, L.; Zhang, Y.; Ferreira, A.; Zhang, L. Magnetite Nanostructured Porous Hollow Helical Microswimmers for Targeted Delivery. *Adv. Funct. Mater.* **2015**, *25*, 5333.

(25) Zhang, L.; Abbott, J. J.; Dong, L.; Kratochvil, B. E.; Bell, D.; Nelson, B. J. Artificial bacterial flagella: Fabrication and magnetic control. *Appl. Phys. Lett.* **2009**, *94*, 064107.

(26) Lin, Z.; Fan, X.; Sun, M.; Gao, C.; He, Q.; Xie, H. Magnetically Actuated Peanut Colloid Motors for Cell Manipulation and Patterning. *ACS Nano* **2018**, *12*, 2539.
(27) Li, J. Y.; Li, X. J.; Luo, T.; Wang, R.; Liu, C. C.; Chen, S. X.; Li, D. F.; Yue, J. B.; Cheng, S. H.; Sun, D. Development of a magnetic microrobot for carrying and delivering targeted cells. *Science Robotics* **2018**, *3*, No. eaat8829.
(28) Xu, H.; Medina-Sánchez, M.; Magdanz, V.; Schwarz, L.; Hebenstreit, F.; Schmidt, O. G. Sperm-Hybrid Micromotor for Targeted Drug Delivery. *ACS Nano* **2018**, *12*, 327.
(29) Medina-Sánchez, M.; Schwarz, L.; Meyer, A. K.; Hebenstreit, F.; Schmidt, O. G. Cellular Cargo Delivery: Toward Assisted Fertilization by Sperm-Carrying Micromotors. *Nano Lett.* **2016**, *16*, 555.
(30) Kim, J.-w.; Jeong, H.-k.; Southard, K. M.; Jun, Y.-w.; Cheon, J. Magnetic Nanotweezers for Interrogating Biological Processes in Space and Time. *Acc. Chem. Res.* **2018**, *51*, 839.
(31) Timonen, J. V. I.; Demirörs, A. F.; Grzybowski, B. A. Magnetofluidic Tweezing of Nonmagnetic Colloids. *Adv. Mater.* **2016**, *28*, 3453.
(32) Timonen, J. V. I.; Grzybowski, B. A. Tweezing of Magnetic and Non-Magnetic Objects with Magnetic Fields. *Adv. Mater.* **2017**, *29*, 1603516.
(33) Xin, C.; Yang, L.; Li, J.; Hu, Y.; Qian, D.; Fan, S.; Hu, K.; Cai, Z.; Wu, H.; Wang, D.; Wu, D.; Chu, J. Conical Hollow Microhelices with Superior Swimming Capabilities for Targeted Cargo Delivery. *Adv. Mater.* **2019**, *31*, 1808226.
(34) Xia, H.; Wang, J.; Tian, Y.; Chen, Q.-D.; Du, X.-B.; Zhang, Y.-L.; He, Y.; Sun, H.-B. Ferrofluids for Fabrication of Remotely Controllable Micro-Nanomachines by Two-Photon Polymerization. *Adv. Mater.* **2010**, *22*, 3204.
(35) Yang, L.; Chen, X.; Wang, L.; Hu, Z.; Xin, C.; Hippler, M.; Zhu, W.; Hu, Y.; Li, J.; Wang, Y.; Zhang, L.; Wu, D.; Chu, J. Targeted Single-Cell Therapeutics with Magnetic Tubular Micromotor by One-Step Exposure of Structured Femtosecond Optical Vortices. *Adv. Funct. Mater.* **2019**, *29*, 1905745.
(36) Urban, A. S.; Lutich, A. A.; Stefani, F. D.; Feldmann, J. Laser Printing Single Gold Nanoparticles. *Nano Lett.* **2010**, *10*, 4794.
(37) Nedev, S.; Urban, A. S.; Lutich, A. A.; Feldmann, J. Optical Force Stamping Lithography. *Nano Lett.* **2011**, *11*, 5066.
(38) Gargiulo, J.; Brick, T.; Violi, I. L.; Herrera, F. C.; Shibanuma, T.; Albella, P.; Requejo, F. G.; Cortés, E.; Maier, S. A.; Stefani, F. D. Understanding and Reducing Photothermal Forces for the Fabrication of Au Nanoparticle Dimers by Optical Printing. *Nano Lett.* **2017**, *17*, 5747.
(39) Lin, L.; Lepeshov, S.; Krasnok, A.; Jiang, T.; Peng, X.; Korgel, B. A.; Alù, A.; Zheng, Y. All-optical reconfigurable chiral meta-molecules. *Mater. Today* **2019**, *25*, 10.
(40) Lin, L.; Zhang, J.; Peng, X.; Wu, Z.; Coughlan, A. C. H.; Mao, Z.; Bevan, M. A.; Zheng, Y. Opto-thermophoretic assembly of colloidal matter. *Science Advances* **2017**, *3*, No. e1700458.
(41) Lin, L.; Peng, X.; Zheng, Y. Reconfigurable opto-thermoelectric printing of colloidal particles. *Chem. Commun.* **2017**, *53*, 7357.
(42) Ergeneman, O.; Peters, C.; Gullo, M. R.; Jacot-Descombes, L.; Gervasoni, S.; Özkale, B.; Fatio, P.; Cadarso, V. J.; Mastrangeli, M.; Pané, S.; Brugger, J.; Hierold, C.; Nelson, B. J. Inkjet printed superparamagnetic polymer composite hemispheres with programmed magnetic anisotropy. *Nanoscale* **2014**, *6*, 10495.
(43) Lin, L.; Peng, X.; Mao, Z.; Li, W.; Yogeesh, M. N.; Rajeeva, B. B.; Perillo, E. P.; Dunn, A. K.; Akinwande, D.; Zheng, Y. Bubble-Pen Lithography. *Nano Lett.* **2016**, *16*, 701.
(44) Zheng, Y.; Liu, H.; Wang, Y.; Zhu, C.; Wang, S.; Cao, J.; Zhu, S. Accumulating microparticles and direct-writing micropatterns using a continuous-wave laser-induced vapor bubble. *Lab Chip* **2011**, *11*, 3816.
(45) Xie, Y.; Zhao, C. An optothermally generated surface bubble and its applications. *Nanoscale* **2017**, *9*, 6622.
(46) Bangalore Rajeeva, B.; Lin, L.; Perillo, E. P.; Peng, X.; Yu, W. W.; Dunn, A.; Zheng, Y. High-Resolution Bubble Printing of Quantum Dots. *ACS Appl. Mater. Interfaces* **2017**, *9*, 16725.
(47) Armon, N.; Greenberg, E.; Layani, M.; Rosen, Y. S.; Magdassi, S.; Shpaisman, H. Continuous Nanoparticle Assembly by a Modulated Photo-Induced Microbubble for Fabrication of Micrometric Conductive Patterns. *ACS Appl. Mater. Interfaces* **2017**, *9*, 44214.
(48) Edri, E.; Armon, N.; Greenberg, E.; Hadad, E.; Bockstaller, M. R.; Shpaisman, H. Assembly of Conductive Polyaniline Microstructures by a Laser-Induced Microbubble. *ACS Appl. Mater. Interfaces* **2020**, *12*, 22278.
(49) Gençer, A.; Schütz, C.; Thielemans, W. Influence of the Particle Concentration and Marangoni Flow on the Formation of Cellulose Nanocrystal Films. *Langmuir* **2017**, *33*, 228.
(50) Ye, J. Y.; Chang, G.; Norris, T. B.; Tse, C.; Zohdy, M. J.; Hollman, K. W.; O'Donnell, M.; Baker, J. R. J. O. l. Trapping cavitation bubbles with a self-focused laser beam. *Opt. Lett.* **2004**, *29*, 2136.
(51) Zhao, C.; Xie, Y.; Mao, Z.; Zhao, Y.; Rufo, J.; Yang, S.; Guo, F.; Mai, J. D.; Huang, T. J. Theory and experiment on particle trapping and manipulation via optothermally generated bubbles. *Lab Chip* **2014**, *14*, 384.
(52) Ni, S.; Leemann, J.; Wolf, H.; Isa, L. Insights into mechanisms of capillary assembly. *Faraday Discuss.* **2015**, *181*, 225.
(53) Stanton, M. M.; Park, B.-W.; Miguel-López, A.; Ma, X.; Sitti, M.; Sánchez, S. Biohybrid Microtube Swimmers Driven by Single Captured Bacteria. *Small* **2017**, *13*, 1603679.

https://dx.doi.org/10.1021/acs.nanolett.0c04165
Nano Lett. 2021, 21, 1628−1635